Available online at www.sciencedirect.com

SciVerse ScienceDirect

Acta Materialia 60 (2012) 6952–6960

Acta MATERIALIA

www.elsevier.com/locate/actamat

Hidden order in the fracture surface morphology of metallic glasses

M. Gao, B.A. Sun, C.C. Yuan, J. Ma, W.H. Wang *

Institute of Physics, Chinese Academy of Sciences, Beijing 100190, People's Republic of China

Received 8 July 2012; received in revised form 25 August 2012; accepted 27 August 2012
Available online 3 October 2012

Abstract

We report the fractal nature of dimple structures on the fracture surface of various metallic glasses (MGs) with significantly different mechanical properties. The analyzed fractal dimension increments of MGs lie in a narrow range of 0.6–0.8. The results indicate that the MGs with marked differences in plasticity and toughness may have a unified local softening mechanism and similar nonlinear plastic behavior in front of the crack tip during fracture. We present a physical picture for the dimple structure formation from the plastic zone in front of the crack tip. The evolution of the plastic zone from the interaction of the shear transformation zones is theoretically modeled as a stochastic process far from thermodynamic equilibrium, and the model can capture the formation and fractal nature of the dimple structures on the fracture surface of metallic glasses.

Keywords: Metallic glass; Fracture surface morphology; Fractal nature of dimple structure

1. Introduction

The fracture surface of glasses has a complicated morphology. Investigation of the fracture morphology and surface roughening phenomena is one of the most direct and effective methods to understand the fracture behavior and mechanism of materials because abundant fracture information is stored on the surface of fracture [1–3]. One of the enduring attractions of metallic glasses (MGs) is their diverse and impressive mechanical properties, which have been proven to be of fundamental scientific and industrial interest [4,5]. For example, the fracture toughness, K_C, varies significantly from 1.26 MPa $m^{1/2}$ for Dy-based MGs [5], which is almost close to the value for ideal brittle oxide glasses [6], to 200 MPa $m^{1/2}$ for Pd-based MGs, which exhibit the highest known damage tolerance [7]. Moreover, the Young's modulus E varies from 16.0 GPa for Zn-based MGs to 246.9 GPa for Co-based MGs [5]. It is intriguing to see whether these MGs have unified or different fracture mechanisms and characteristics.

Diverse patterns such as dimple structures [8,9], periodic corrugations [10] and river patterns [9] have been observed on the fracture surface of different MGs. Some nanoscale structures such as nanocones, nanospheres and nanowires were also observed on the fracture surfaces of MGs [11]. Thus, MGs are good model systems for studying the origin of fracture surface roughening in disordered glassy materials. In particular, the characteristic morphology of the dimple network-like structure on fracture surfaces may be a fingerprint to discover hidden information in the fracture process of MGs. However, previous researches [8,9] have mainly focused on the average dimple size and seldom involved the spatial distribution of dimple structures, and the fracture mechanism of MGs remains a mystery.

The concept of fractals was first introduced into materials science by Mandelbrot et al. [12] to study the statistical characteristics of some irregular, rough or fragmented geometric shapes. A fractal object is often characterized by a fraction dimension, the fractal dimension D, in contrast to the integral number for a Euclidean. The fractal dimension has proved to be one of the most significant parameters for characterization of the surface topography and can provide quantitative topographical information [13].

* Corresponding author.
E-mail address: whw@iphy.ac.cn (W.H. Wang).

1359-6454/$36.00
http://dx.doi.org/10.1016/j.actamat.2012.08.046

D is insensitive to structural details, and thus provides a comprehensive description on the degree of complexity of various surface morphologies [14]. However, little work has been done on fracture morphology in MGs using the fractal geometry analysis method.

In this paper, we systematically investigate the dimple network-like structure on the fracture surface of 12 MGs with significantly different toughness (K_C ranging from 1.26 to 200 MPa $m^{1/2}$) using the fractal geometry analysis method, in an effort to extract the hidden order in these seemingly random and complex patterns on the fracture surface. Strikingly, our results reveal that the fracture surface of MGs has a far more complex structure than that commonly seen, which shows a fractal characteristic. Furthermore, the fractal dimensions of the dimple network-like structures measured for various MGs seem to be a constant under the same external conditions, indicating that a unified fracture mechanism may exist for these MGs with markedly different mechanical properties. A possible theoretical scenario to understand the fractal nature from the plastic zone ahead of the crack tip and the nature of far-from-thermodynamic equilibrium is proposed.

2. Analysis and experimental method

2.1. Fractal analysis method: box-counting method

In general, there are many ways to measure the fractal dimension D [12,15–18]. Although slight differences may exist in the fractal dimension values obtained from different methods, the variation tendency is found to be uniform [13]. In this work, the most common method in fractal analysis, the box-counting method [19], is used to estimate the fractal dimension of the dimple network-like structure on the fracture surface of MGs. For grids of square boxes with edge length Δx, the number of $N(\Delta x)$ of boxes covering at least one pixel of the binary black-and-white image corresponding to the original gray-scale scanning electron microscopy (SEM) image of the dimple structure has the power-law relation of $N(\Delta x) \sim \Delta x^{-D_B}$, where D_B is a typical non-integer number (the physically meaningful values lie between 1 and 2 in two dimensions (2-D), and between 2 and 3 in 3-D) called the "box-counting" dimension for a fractal object. In the log–log plot of $N(\Delta x) - \Delta x$, the slope is the fractal dimension D_B.

2.2. Experimental details

All the MGs were prepared by induction melting a mixture of pure metal elements and then casting into a copper mold to form rod-shaped specimens with a diameter of 5 mm and a length of 60 mm [5]. The glass nature of specimens was checked by X-ray diffraction and differential scanning calorimetry. The three-point bending tests were carried out in an Instron 3384 machine (Norwood, MA) with a crosshead moving speed of 0.5 mm min^{-1} at room temperature. Specimens for pre-notched three-point bending tests had a geometric size of 5×30 mm. A diamond saw was used to introduce a notch (250 μm in width and 1.5 mm in depth) in the middle of the cylinders. The newly generated crack surfaces were observed by SEM conducted in a Philips XL30 instrument.

3. Results

3.1. SEM image of the dimple network-like structure of MGs

Figs. 1 and 2 show typical SEM images of the dimple network-like structure on the fracture surface of MGs with the K_C below and above 30 MPa $m^{1/2}$, respectively. The average dimple size estimated from these images increases with the toughness of the MGs from the nanometer scale in brittle Dy- and Mg-based MGs to the millimeter scale in tough Pd-based MGs, which agrees well with the previous experimental results [9]. Fig. 3 shows the fracture profile and three detailed morphologies corresponding to three different zones I, II, III in the dimple region of the fracture surface of $Zr_{41}Ti_{14}Cu_{12.5}Ni_{10}Be_{22.5}$. One can clearly see that the average dimple size cannot effectively and completely characterize the fracture characteristics of these MGs. In particular, these dimple structures are remarkably irregular and complex, and appear at different length scales, which seems difficult to describe in terms of Euclidean geometry.

3.2. Fractal dimension of the dimple network-like structure of MGs

Based on the box-counting method, the original gray-scale SEM micrographs are first digitized into the binary black-and-white images by applying the median filter method, as illustrated in Fig. 4. By comparing Figs. 1a and 2a with Fig. 4a and b, one can clearly see that the binary black-and-white images maintain the fundamental characteristics of the original gray-scale SEM micrographs of dimple structures. Therefore, the original gray-scale SEM images (as well as the median-filtered images) analysis method is suitable and valid for analysis of the fracture surfaces of MGs. For grids of square boxes with edge length Δx, the number of boxes $N(\Delta x)$ covering at least one pixel of the wall of dimple structure is counted. Fig. 5 shows the log–log plots of the number of box $N(\Delta x)$ vs. the size of box Δx for binary black-and-white images of $Dy_{40}Y_{16}Al_{24}Co_{20}$ and $Zr_{61}Ni_{12.8}Al_{7.9}Cu_{18.3}$, two alloys that exhibit very different toughness and plasticity. A clear linear scaling regime extending more than three orders of magnitude of Δx can be seen in the intermediate part of the plots, which is a typical feature of a fractal. Deviations from the linear region at both ends are also observed, often arising from the finite size effect of actual fractal objects [19].

To ensure the accuracy of the fractal dimension of the dimple structure, we make a systematic error bar analysis for the fractal analysis of dimple structures of all MGs. Firstly, we select three zones of the same size in the dimple

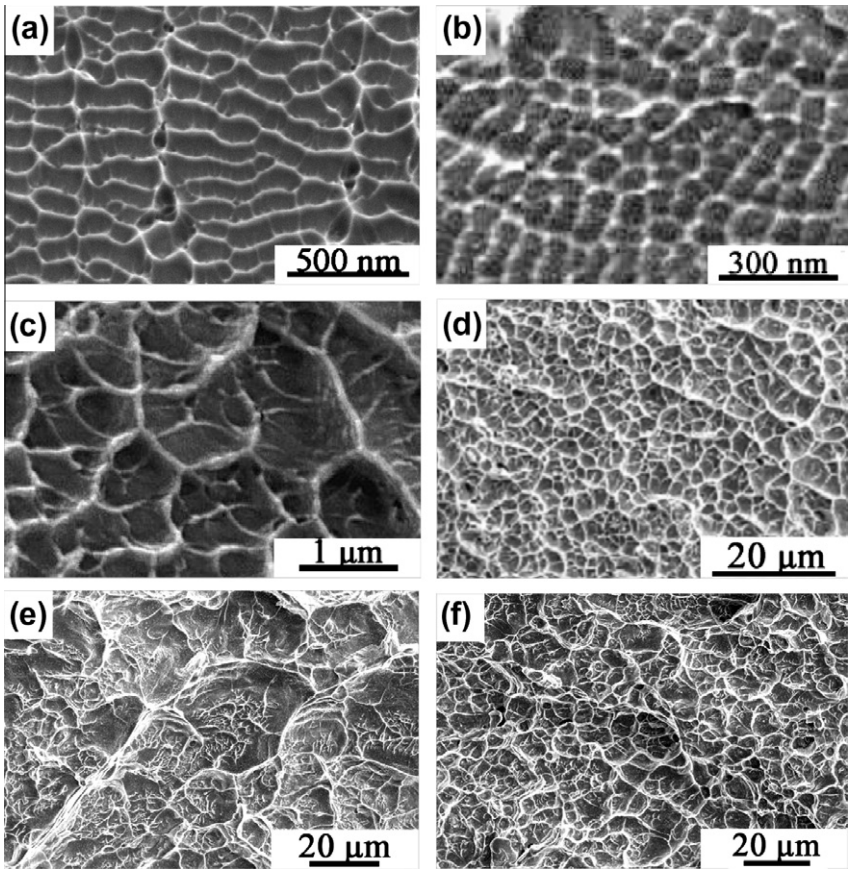

Fig. 1. SEM image of the dimple structure on the fracture surface of MGs with fracture toughness K_C below 30 MPa $m^{1/2}$: (a) $Dy_{40}Y_{16}Al_{24}Co_{20}$; (b) $Mg_{65}Cu_{25}Gd_{10}$ [9]; (c) $La_{55}Al_{25}Cu_{10}Ni_5Co_5$ [21]; (d) $Ce_{60}Al_{20}Ni_{10}Cu_{10}$ [9]; (e) $Zr_{52.5}Cu_{17.9}Ni_{14.6}Al_{10}Ti_5$; (f) $Zr_{57}Nb_5Cu_{15.4}Ni_{12.6}Al_{10}$.

region on the fracture surface of MGs (e.g. $Zr_{41}Ti_{14}Cu_{12.5}Ni_{10}Be_{22.5}$, see Fig. 3). For each selected zone, we make different transitions from the original gray-scale SEM micrographs to the binary black-and-white images by using three different median filter values. We then obtain the fractal dimensions by the box-counting method. Thus, the error bar includes three parts: the error from different sites in dimple region, the error from the SEM image-binary image transition process, and the error from the box-counting method. In Fig. 5a and b, $m = 0.027$ and $m = 0.026$ are the fitting standard errors from the box-counting method. Considering the other two parts of errors, the values of D of $Dy_{40}Y_{16}Al_{24}Co_{20}$ and $Zr_{61}Ni_{12.8}Al_{7.9}Cu_{18.3}$ are determined to be 1.632 ± 0.065 and 1.757 ± 0.050, respectively. Similar analyses show that the dimple structures of other MGs also exhibit fractal characteristics, and the measured D values are listed in Table 1.

Fig. 6 shows the summary of the fractal dimension increment D^* ($D^* = D - 1$) vs. K_C of these MGs. The values of D^* lie in a narrow range of 0.6–0.8, and the average D^* is about 0.70 for all the studied MGs. All D values are similar and between 1 and 2 in the 2-D surface, indicating a typical fractal characteristic for MGs with significantly different mechanical properties. It is noted that the dimple structure on the fracture surface has 3-D topography and what we measured here is in fact the fractal dimension of the 2-D in-plane projection of the dimple network. According to the fractal theory, the real fractal dimension D_R for the 3-D dimple structure should be $D_R = D + 1$. The fractal dimension seems not to depend on the chemical composition and mechanical properties of these MGs. The constant of the measured fractal dimension suggests that the dimple structures are self-similar and have no characteristic length scale for MGs, which are only limited by their toughness. Recently, the self-affine or power-law scaling was also obtained by Bouchoud et al. [26] from the roughness analysis of the fracture surface of a Zr-based MG, where they obtained a scaling exponent $\beta = 0.55$. The value agrees well with our present analysis on the fractal dimension from the relation $\beta = 3 - D_R = 2 - D$. The fractal nature of the fracture surface has also been reported in other brittle materials where dimple structures are not observed. In contrast to MGs, the fractal dimensions for these materials are highly scattered and have been found to be closely related with the mechanical properties [27]. The fractal nature and the similar fractal dimension suggest that MGs with diverse mechanical properties from extreme brittle to the most tough may have a unified fracture mechanism.

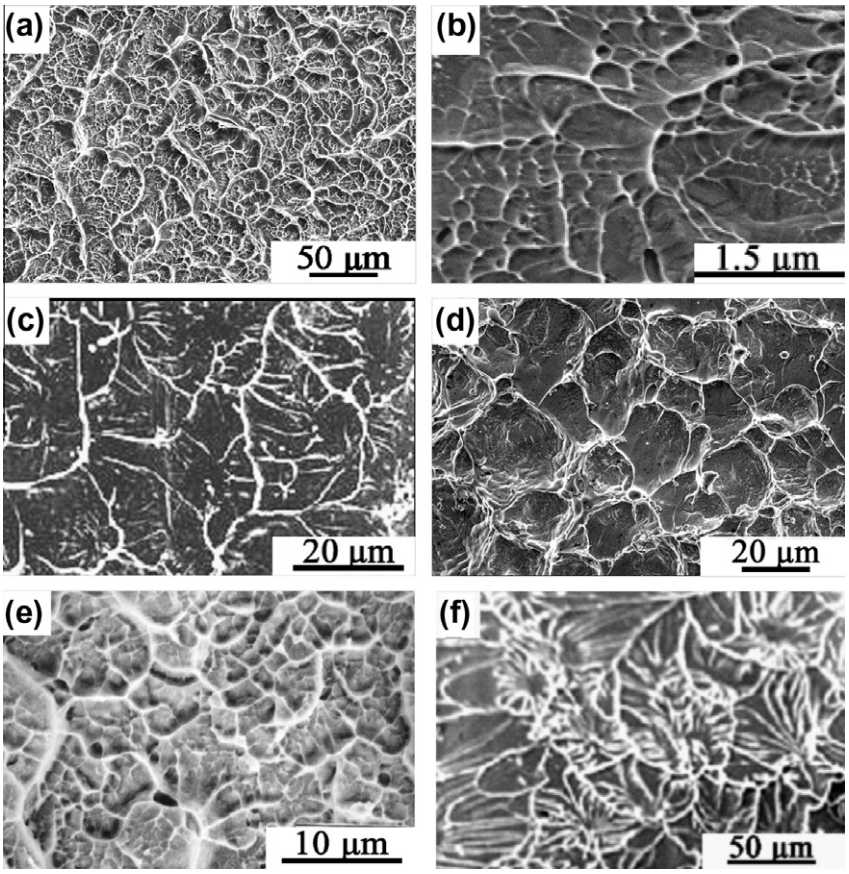

Fig. 2. SEM image of the dimple structure on the fracture surface of MGs with the K_C above 30 MPa $m^{1/2}$: (a) $Zr_{61}Ni_{12.8}Al_{7.9}Cu_{18.3}$; (b) $Fe_{66}Cr_3Mo_{10}P_8C_{10}B_3$ [25]; (c) $Ti_{50}Ni_{24}Cu_{20}B_1Si_2Sn_3$ [9]; (d) $Zr_{57}Ti_5Cu_{20}Ni_8Al_{10}$; (e) $Zr_{41}Ti_{14}Cu_{12.5}Ni_{10}Be_{22.5}$ [8]; (f) $Pd_{79}Ag_{3.5}P_6Si_{9.5}Ge_2$ [7].

4. Discussions

4.1. Physical picture for the formation of dimple structures

Generally, the dimple structures that exist during fracture in MGs are closely related to the local softening process in the plastic zone ahead of crack tip, i.e. the meniscus instability [28]. As the crack tip is stable, theoretical analysis [29] showed that the size of plastic zone could have a stable length scale. However, our fractal analysis clearly suggests that the situation during the fracture of MGs is much more complex. Specifically, the fractal nature of these dimple structures suggests that MG fracture is a far-from-equilibrium process, and a dissipation structure in nonlinear dynamics may have formed. Thus, the fractal nature must be closely related to the nonlinear deformation process in the plastic zone ahead of the crack tip during fracture of MGs. Here, for simplicity, we try to understand the fractal formation process from a stochastic version of shear transformation theory based on the similarity between the formation of the shear band in plastic deformation of MGs and the plastic zone of the crack tip in the fracture of MGs.

Both the shear band and the plastic zone are formed due to the stress localization and the local shear softening during the deformation of MGs, which is confirmed by many experimental results [9,10,30–32]. As for the formation of the shear band, Langer et al. [33] offered a reasonable explanation based on STZ theory. Accordingly, we assumed similarly that the operation of these STZs creates a localized softening of the surrounding material and triggers the autocatalytic formation of more STZs in the crack tip during fracture. The organization of STZs coalesces together into a softening zone—the plastic zone—which corresponds to the dimple structure after fracture. The size of the plastic zone can be then assumed to be proportional to the number of STZs [34,35]. Hence, the power scaling of dimple size in fact indicates the scaling of the size of STZ aggregations. In this regard, the interaction or spatial correlation among STZs should be considered in the crack-tip during the fracture. In fact, in the quasi-static limit, Maloney and Lemaitre [36] have shown by simulation that a localized elastic disturbance generated by a single STZ flip can lead to an avalanche of spatially correlated STZ arrangements. Langer [37] also showed that the elementary shear transformation is associated with quadrupolar energy fluctuation, and the consequent long-range elastic stress field between STZs can induce strain localization and fracture in glassy materials. Based on the above analysis, a microscopic picture with the interaction of STZs for

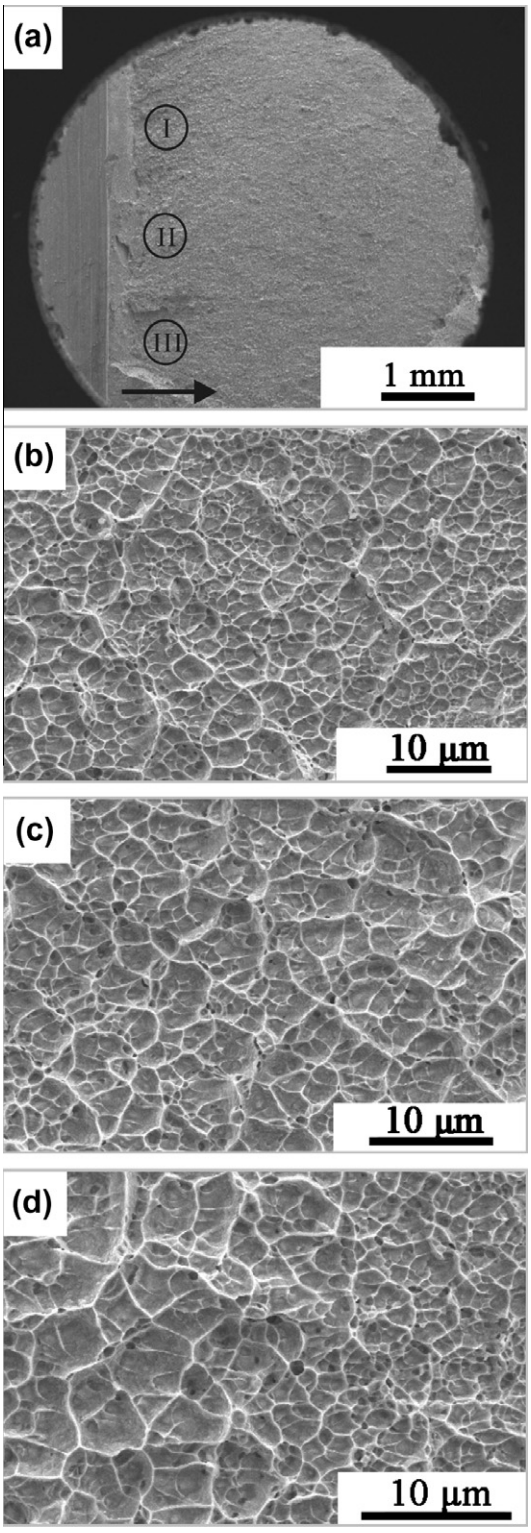

Fig. 3. Fracture profile of $Zr_{41}Ti_{14}Cu_{12.5}Ni_{10}Be_{22.5}$ under three-point bending fracture. (a) Overview of the fracture surface (the black arrow indicates the crack propagation direction and I, II, III represent the selected three zones in the dimple region). (b) Detailed morphology corresponding to zone I in (a). (c) Detailed morphology corresponding to zone II in (a). (d) Detailed morphology corresponding to zone III in (a).

the formation of dimple structure is proposed, as shown in Fig. 7. The crack tip open distance (CTOD), which is

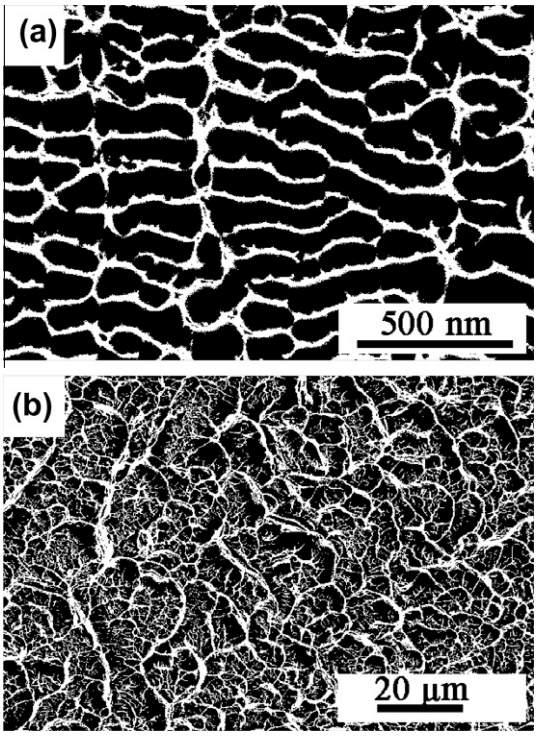

Fig. 4. Binary black-and-white image from the original gray-scale SEM micrograph of two various MGs by the median filter: (a) $Dy_{40}Y_{16}Al_{24}Co_{20}$; (b) $Zr_{61}Ni_{12.8}Al_{7.9}Cu_{18.3}$.

associated with the critical stress intensity factor, is also plotted in Fig. 7.

4.2. Simple stochastic model for the spatial evolution of dimples from correlated STZs

To further understand the formation and fractal nature of the dimple network-like structures theoretically, we propose a simple stochastic model for the spatial evolution of correlated STZs in the plastic zone at the crack tip of MGs based on the above physical picture of the formation of dimple structures and the athermal STZ theory [33]. In this model, we consider collective STZ evolution in plastic zone as a stochastic process far from thermodynamic equilibrium. According to the athermal STZ theory (for simplicity, we only consider the scalar version of STZ theory), we assume that STZs in the plastic zone at the crack tip of MGs are two-state systems, which, in the presence of a pure shear stress s, can switch back and forth between only two orientations. During the fracture of MGs, with the effect of the shear stress s, some STZs can be activated and all these STZs lie in the two states, backward and forward. Due to the heterogeneity of the structure of MGs and the stress localization, some STZs are influenced by a large stress and the other STZs may be affected by a small stress. The heterogeneity of the stress state in the plastic zone leads to the operation and annihilation of STZs and then causes the heterogeneity of the spatial distribution of STZs in the plastic zone. In view of the above physical

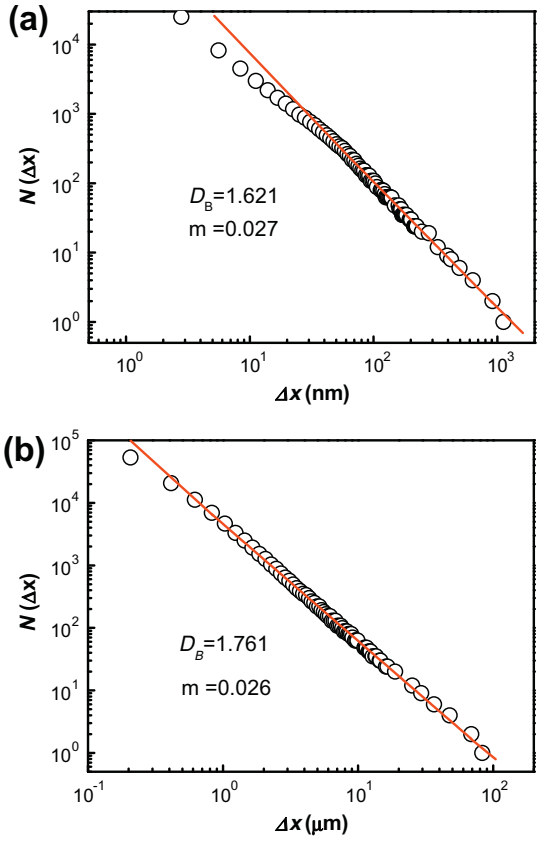

Fig. 5. Log–log plot of the number of box $N(\Delta x)$ vs. the size of box Δx of binary black-and-white images of $Dy_{40}Y_{16}Al_{24}Co_{20}$ (a) and $Zr_{61}Ni_{12.8}Al_{7.9}Cu_{18.3}$ (b). The value of m represents the fitting standard error of the box-counting method.

Table 1
The fracture toughness K_C and the fractal dimension D of MGs.

Metallic glasses	K_C (MPa m$^{1/2}$)	D	Refs.
$Dy_{40}Y_{16}Al_{24}Co_{20}$	1.26	1.632 ± 0.065	[20]
$Mg_{65}Cu_{25}Gd_{10}$	2	1.647 ± 0.052	[9]
$La_{55}Al_{25}Cu_{10}Ni_5Co_5$	5	1.680 ± 0.039	[21]
$Ce_{60}Al_{20}Ni_{10}Cu_{10}$	10	1.739 ± 0.041	[9]
$Zr_{52.5}Cu_{17.9}Ni_{14.6}Al_{10}Ti_5$	20	1.748 ± 0.035	[22]
$Zr_{57}Nb_5Cu_{15.4}Ni_{12.6}Al_{10}$	27	1.731 ± 0.039	[23]
$Zr_{61}Ni_{12.8}Al_{7.9}Cu_{18.3}$	39.8	1.757 ± 0.050	[24]
$Fe_{66}Cr_3Mo_{10}P_8C_{10}B_3$	46.7	1.663 ± 0.048	[25]
$Ti_{50}Ni_{24}Cu_{20}B_1Si_2Sn_3$	50	1.668 ± 0.060	[6]
$Zr_{57}Ti_5Cu_{20}Ni_8Al_{10}$	80	1.694 ± 0.070	[24]
$Zr_{41}Ti_{14}Cu_{12.5}Ni_{10}Be_{22.5}$	86	1.653 ± 0.044	[8]
$Pd_{79}Ag_{3.5}P_6Si_{9.5}Ge_2$	200	1.678 ± 0.047	[7]

picture of the formation of dimple structures, the more STZs are organized in one place at crack tip, the larger the plastic zone are formed in this place and then the larger the dimples produced on the fracture surface. Therefore, the evolution process of the whole density n of STZs determines the spatial distribution of the dimple structure on the fracture surface of MGs after fracture.

In order to derive the evolution process of the total STZ density theoretically, we introduce some variables. We define n_+ and n_- as the population density of STZs in

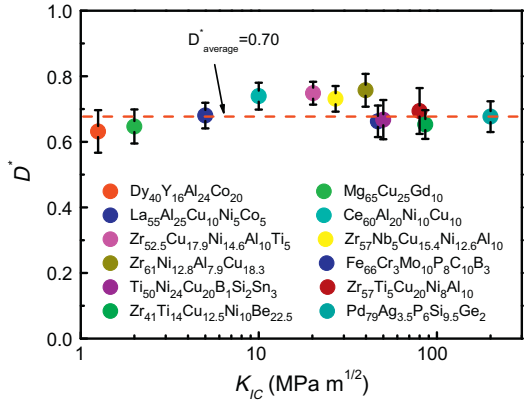

Fig. 6. Fractal dimension increment $D^* = D - 1$ vs. K_C of 12 MGs. The red dashed line represents the average D^* value (0.70) for studied MGs.

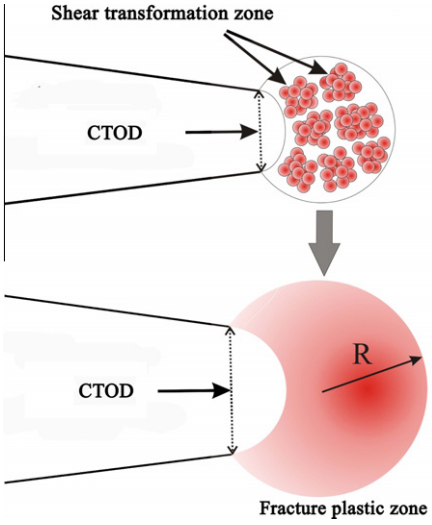

Fig. 7. Sketch of the formation mechanism of the fracture plastic zone in front of the crack tip. Below is the stress distribution schema in the fracture plastic zone at the crack tip. The deeper color indicates the larger stress. R is the size of the fracture plastic zone and CTOD represents the "crack tip open distance".

two states, forward and backward, respectively. In addition, we define an internal state variable $\Lambda = (n_+ + n_-)/n_\infty$ as the total STZ density, where n_∞ is the natural density limit for n, the total density of STZs, in the plastic zone at the crack tip during fracture. According to the athermal STZ theory [33], we can obtain the master function for the whole density Λ of STZs without the interaction of STZs:

$$\tau_0 \dot{\Lambda} = \Gamma(e^{-1/\chi} - \Lambda), \quad (1)$$

where τ_0 sets a time scale for the molecular rearrangement; $\Gamma/\tau_0$is the rate at which STZs are created and annihilated and can be regarded as proportional to the energy dissipation rate per STZ: $\Gamma/\tau_0 = sD_{pl}/\Lambda\,\epsilon_0$, where D_{pl} is the strain rate and ϵ_0 is a constant representing the number of STZs in a specific volume; χ is a dimensionless variable and is considered as the reduced effective temperature by the units

of STZ formation energy [33], $\chi = T_{eff}(k_B/E_{STZ}) = T_{eff}k_B/E_{STZ}$, where E_{STZ} is the characteristic STZ formation energy, T_{eff} is the true effective temperature and k_B is the Boltzmann constant. χ evolves with deformation by $\tau_0 c_0 \dot{\chi} = \epsilon_0 \Gamma \Lambda(\chi_\infty - \chi)$, where c_0 is the specific heat and χ_∞ is the steady-state value of χ.

From Eq. (1), we can see that the STZs in the absence of spatial correlation can operate under a steady-state stress $s_{ste} = s$, which can be regarded as a smooth function in space and time, and χ can also evolve into its steady-state value χ_∞. In this case, the probability of finding STZs should be accurately proportional to a Boltzmann factor of $\exp(-E_{STZ}/k_B T_{eff}) = \exp(-1/\chi)$. In our present study and based on the assumption of the formation of the dimple structure, however, the distribution of STZ density (measured as the number of atoms involved in the localized irreversible plastic deformation) obeys a power law, implying that the system has been far from equilibrium during the persistent deformation and that the interaction between STZs should be considered.

Here, we consider that the transient STZ interaction via long-range elastic stress field can induce the fluctuating internal stress s_{int} on operating STZs, and thus the effective stress s_{eff} acting on STZ is $s_{eff} = s_{ste} + s_{\text{int}}$. The noise character s_{int} gives rise to the spatiotemporal variation of plastic strain rate, and then causes a change in the spatial distribution of STZ density.

Now we allow the stress s and plastic strain rate D_{pl} to fluctuate in order to take into consideration the effect of the interaction between STZs: $s_{eff} = s_{ste} + \delta s_{eff}$, $D_{pl} = \langle D_{pl}\rangle + \delta D_{pl}$. For similarity, the strain-rate fluctuations δD_{pl} are approximated by a stationary Gauss white noise with zero mean [38]: $\delta D_{pl} = \sqrt{\tau\langle \delta D_{pl}^2\rangle}\delta w$, where $\delta w(t)\delta w(t') = \delta(t - t')$ and τ is the correlation time of STZs, and the stress fluctuation δs_{eff} is the internal stress noise s_{int}. Defining the strain-rate sensitivity $S = \partial \ln \langle s_{eff}\rangle / \partial \ln \langle D_{pl}\rangle$ [39], we have $\delta s_{eff} = S(\delta D_{pl}/\langle D_{pl}\rangle)\langle s_{eff}\rangle$. Taking the expression of the s_{eff} and D_{pl} into Eq. (1), we obtain the dynamic evolution function for the whole density Λ of STZs considering the interaction of STZs:

$$\tau_0 \dot{\Lambda} = \frac{\rho}{\epsilon_0}\left(\frac{\Lambda_\infty}{\Lambda} - 1\right) + \frac{\varphi}{\epsilon_0}\left(\frac{\Lambda_\infty}{\Lambda} - 1\right)\delta w, \tag{2}$$

where $\Lambda_\infty = \exp(-1/\chi_\infty)$, $\rho = \langle s_{eff}\rangle\langle D_{pl}\rangle$, and $\varphi = \langle s_{eff}\rangle \times (1+S)\sqrt{\frac{\tau\langle s_{\text{int}}\rangle\langle D_{pl}\rangle}{S}}$. Eq. (2) is a typical Langevin equation. Statistical information about STZ distribution can be obtained from the Fokker–Planck equation corresponding to Eq. (2). Define $h(\Lambda) = \frac{\rho}{\epsilon_0\tau_0}\left(\frac{\Lambda_\infty}{\Lambda} - 1\right), g(\Lambda) = \frac{\varphi}{\epsilon_0\tau_0}\left(\frac{\Lambda_\infty}{\Lambda} - 1\right)$ and use the Stratonovich calculus [40] to yield:

$$\frac{\partial p(\Lambda,t)}{\partial t} = -\frac{\partial}{\partial \Lambda}\left[\left(h(\Lambda) + \frac{1}{2}g(\Lambda)\frac{\partial}{\partial}g(\Lambda)\right)p(\Lambda,t)\right] + \frac{1}{2} \times \frac{\partial^2}{\partial \Lambda^2}\left[g^2(\Lambda)p(\Lambda,t)\right], \tag{3}$$

where $p(\Lambda, t)$ is the probability density distribution function of Λ at time t. With the evolution of stochastic dynamics, $p(\Lambda, t)$ will evolve into a stationary probability density from the steady-state solution of Eq. (3):

$$p_s(\Lambda) = \frac{N'}{g(\Lambda)}\exp\left[2\int_0^\Lambda \frac{h(\Lambda)}{g^2(\Lambda)}d\Lambda\right], \tag{4}$$

where N' is a normalization constant chosen based on $\int p_s(\Lambda)d\Lambda = 1$. Taking the specific expressions of $h(\Lambda)$, $g(\Lambda)$ into Eq.(4), we obtain:

$$p_s(\Lambda) = N\Lambda^{-2\sigma\Lambda_\infty}\left(\frac{\Lambda_\infty}{\Lambda} - 1\right)^{-(1+2\sigma\Lambda_\infty)}\exp(-2\sigma\Lambda), \tag{5}$$

where N is again a normalization constant and $\sigma = \rho\tau_0 \epsilon_0/\varphi^2$(a constant parameter). As in the steady state, Λ is very close to Λ_∞, and thus $(\Lambda_\infty/\Lambda - 1)$ varies very slowly compared to Λ; this reduces $p_s(\Lambda)$ to:

$$p_s(\Lambda) \sim \Lambda^{-2\sigma\Lambda_\infty}\exp(-2\sigma\Lambda). \tag{6}$$

Considering the expression of ρ and φ, σ is transformed into:

$$\sigma = \tau_0\epsilon_0 S/(\tau\langle s_{eff}\rangle(1+S)^2\langle s_{\text{int}}\rangle). \tag{7}$$

From above discussion on the formation of the dimple structure, the size of dimple structure λ should be proportional to $\Lambda^{1/2}$. Eq. (6) is then transformed into a dimple size distribution by a change of variables of $p_s(\Lambda)d\Lambda = p_s(\lambda)d\lambda$:

$$p_s(\lambda) \sim \lambda^{-\beta}\exp(-2\sigma\lambda^2) \tag{8}$$

with $\beta = 4\sigma\Lambda_\infty - 1$.

4.3. Discussions on the stochastic model for the spatial evolution of dimples from correlated STZs and experimental results

To investigate the spacing size evolution of the STZ distribution, we study the qualitative changes in $p_s(\lambda)$ when the noise σ increases from small to large values with different values of Λ_∞, as illustrated in Fig. 8. Fig. 8a shows a qualitative change of $p_s(\lambda)$ when the noise σ increases with $\Lambda_\infty = 1$. One can see that for the value of $\Lambda_\infty = 1$, when $\sigma < 0.25$, the probability distributions possess different maxima in the vicinity of the deterministic steady-state with different values of σ, while they fall off to zero both for $\sigma = 0$ and $\sigma = \infty$. At the critical value $\sigma = 0.25$, a monotonically decreasing probability distribution appears. For $\sigma > 0.25$, a hyperbolic distribution appears and the exponential term $\exp(-2\sigma\lambda^2)$ becomes trivial, which makes $p_s(\lambda)$ diverge to a power scaling $\lambda^{-\beta}$. The value of β should be given and compared with the experimental results D. Similarly, we also find the similar evolution tendency with other values of $\Lambda_\infty = 0.1, 0.01, 0.001$ (see Fig. 8b–d). From analysis above, the power law of the dimple size distribution appears when the noise intensity (or the interaction intensity) satisfies $\sigma > 1/4\Lambda_\infty$. The theoretical analysis confirms that the interaction of STZs leads to the fractal

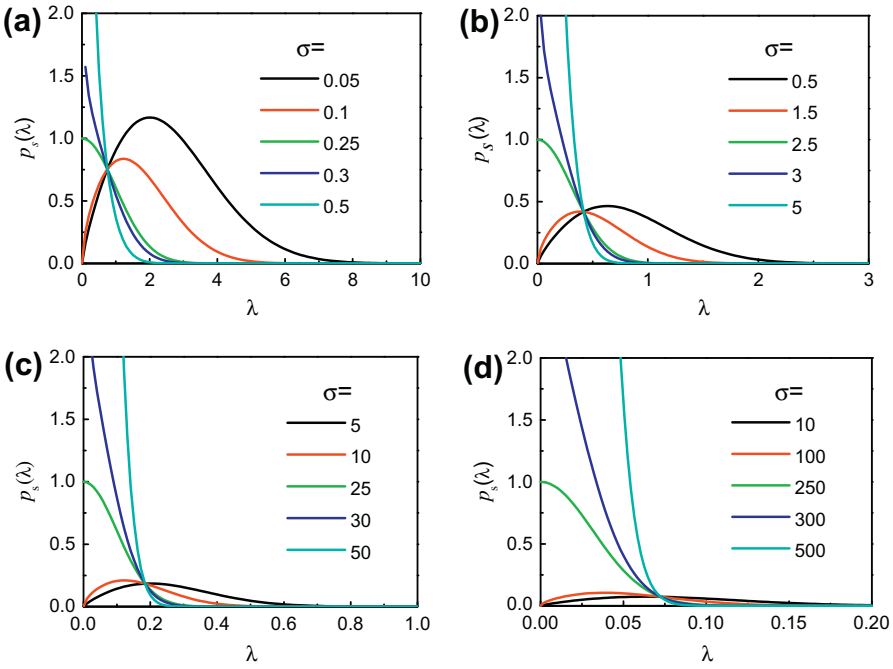

Fig. 8. (a) Steady-state probability distribution of the mean special size of STZ distribution for various values of the noise intensity σ with $\Lambda_\infty = 1$. (b) Steady-state probability distribution of the mean special size of STZ distribution for various values of the noise intensity σ with $\Lambda_\infty = 0.1$. (c) Steady-state probability distribution of the mean special size of STZ distribution for various values of the noise intensity σ with $\Lambda_\infty = 0.01$. (d) Steady-state probability distribution of the mean special size of STZ distribution for various values of the noise intensity σ with $\Lambda_\infty = 0.001$.

distribution of the STZ aggregation in space, and finally forms the fractal dimple network-like structure during fracture.

The observed fluctuation of the fractal dimension D in MGs can be related to the revolution of the various parameters affecting the noise σ. In the region near the notch, the fluctuating internal stress s_{int} is small and the noise σ is then large, which leads to the power-law distribution of the dimple structure. As the crack proceeds, the fluctuating internal stress s_{int} becomes larger and the corresponding noise σ becomes smaller. When the noise $\sigma < 1/4\Lambda_\infty$, the spatial distribution of the dimple structure on the fracture surface transforms from the power-law distribution into the homogeneous distribution, which is confirmed by the spatial evolution of fracture pattern from the dimple structures to the nanoscale periodic stripes [35]. In addition, in view of the dependence of σ on the strain-rate sensitivity S, a wide range of noise levels can be realized for different materials and deformation conditions. Thus, a change in the deformation rate and/or temperature will induce a distribution transition of the dimple structure on the fracture surface.

5. Conclusions

In this study, we demonstrate by both experimental investigations and theoretical analysis that the dimple structure of MGs is fractal. The similar fractal dimensions of various MGs suggest that there is a unified fracture softening mechanism in MGs with different toughness, composition and local plastic flow. Our studies also imply that nonlinear behavior in the crack tip may be a consequence of the coupling between density fluctuation and deformation fields as well as the interaction of STZs, which leads to the complex fracture process. In addition, our method of fracture surface analysis may provide an appropriate tool to find the quantitative relationships between the fracture pattern and the mechanical or structural properties, which is of importance for understanding the fracture mechanism of MGs from their irregular fracture morphology.

Acknowledgements

The work was supported by MOST 973 of China (No. 2010CB731603) and the NSF of China (50921091 and 51271195). The useful discussions and experimental help of D.Q. Zhao and D.W. Ding, and valuable discussions with H.Y. Bai, P. Wen and M.X. Pan are appreciated.

References

[1] Fineberg J, Gross SP, Marder M, Swinney HL. Phys Rev Lett 1991;67:457.
[2] Ramanathan S, Fisher DS. Phys Rev Lett 1997;79:877.
[3] Bonamy D, Ravi-Chandar K. Phys Rev Lett 2004;93:099602.
[4] Schuh CA, Hufnagel TC, Ramamurty U. Acta Mater 2007;55:4067.
[5] Wang WH. Prog Mater Sci 2012;57:487.
[6] Lewandowski JJ, Wang WH, Greer AL. Philos Mag Lett 2005;85:77.
[7] Demetriou MD, Launey ME, Garrett G, Schramm JP, Hofmann DC, Johnson WL, et al. Nat Mater 2011;10:123.
[8] Lowhaphandu P, Lewandowski JJ. Scr Mater 1998;38:1811.
[9] Xi XK, Zhao DQ, Pan MX, Wang WH, Wu Y, Lewandowski JJ. Phys Rev Lett 2005;94:125510.

[10] Wang G, Wang YT, Liu YH, Pan MX, Zhao DQ, Wang WH. Appl Phys Lett 2006;89:121909.
[11] Xia XX, Wang WH, Greer AL. J Mater Res 2009;24:2986.
[12] Mandelbrot BB, Passoja DE, Paullay AJ. Nature 1984;308:721.
[13] Amin JS, Ayatollahi S, Alamdari A. Appl Surf Sci 2009;256:67.
[14] Risović D, Poljaček SM, Gojo M. Appl Surf Sci 2009;255:4283.
[15] Bigerelle M, Iost A. Eng Fract Mech 2004;71:1081.
[16] Pande CS, Richards LE, Louat N, Dempsey BD, Schwoeble AJ. Acta Metall 1987;35:1633.
[17] Li XW, Tian JF, Li SX, Wang ZG. Mater Trans 2001;42:128.
[18] Poljacek SM, Risovic D, Furic K, Gojo M. Appl Surf Sci 2008;254: 3449.
[19] Sun BA, Wang WH. Appl Phys Lett 2011;98:201902.
[20] Wang G, Pan MX, Wu Y, Wang WH. Phys Rev Lett 2007;98:235501.
[21] Nagendar N, Ramamurty U, Goh TT, Li Y. Acta Mater 2000;48: 2603.
[22] Zhang ZY, Keppens V, Liaw PK, Yokoyama Y, Inoue A. J Mater Res 2007;22:364.
[23] Wang WH, Dong C, Shek CH. Mater Sci Eng R 2004;44:45.
[24] Yuan CC, Xi XK. J Appl Phys 2011;109:033515.
[25] Lewandowski JJ, Gu XJ, Nouri AS, Poon SJ, Shiflet GJ. Appl Phys Lett 2008;92:091918.
[26] Bouchaud E, Boivin D, Pouchou JL, Bonamy D, Poon B, Ravichandran G. Europhys Lett 2008;83:66006.
[27] Hill TJ, Mecholsky Jr JJ, Anusavice KJ. J Am Ceram Soc 2000;83: 545.
[28] Xia XX, Wang WH. Small 2012;8:1197.
[29] Argon AS, Salama M. Mater Sci Eng 1976;23:219.
[30] Guan PF, Chen MW, Egami T. Phys Rev Lett 2010;104:205701.
[31] Argon AS. Acta Metall 1979;27:47.
[32] Ashby MF, Greer AL. Scr Mater 2006;54:321.
[33] Langer JS. Phys Rev E 2004;70:041502.
[34] Pan D, Inoue A, Sakurai T, Chen MW. PNAS 2008;105:14769.
[35] Wang YT, Wang G, Xia XX, Wang WH. J Appl Phys 2009;106: 113528.
[36] Maloney C, Lemaître A. Phys Rev Lett 2004;93:016001.
[37] Langer JS. Phys Rev E 2001;64:011504.
[38] Lemaître A, Caroli C. Phys Rev Lett 2009;103:065501.
[39] Hahner P. Appl Phys A 1996;62:473.
[40] Hahner P. Acta Mater 1996;44:2345.